

## The effects of ionospheric outflow on ICME and SIR driven sawtooth events

O. J. Brambles,<sup>1</sup> W. Lotko,<sup>1</sup> B. Zhang,<sup>1</sup> J. Ouellette,<sup>1</sup> J. Lyon,<sup>2</sup> and M. Wiltberger<sup>3</sup>

Received 1 April 2013; revised 15 August 2013; accepted 18 August 2013; published 1 October 2013.

[1] Magnetosphere sawtooth oscillations have been observed during interplanetary coronal mass ejection (ICME) events, when the solar wind conditions are relatively steady, and during periods when the interplanetary magnetic field (IMF) fluctuates between northward and southward, as during interplanetary stream interaction regions (SIR). The impact of ionospheric outflow on the ICME-driven 18 April 2002 and SIR-driven 24 October 2002 sawtooth events is investigated using a multifluid adaptation of the Lyon-Fedder-Mobarry global simulation. The mechanisms that generate the sawtooth oscillations are investigated by comparing a baseline simulation without outflow and a simulation that includes an O<sup>+</sup> outflow model. The ionospheric outflow is regulated by a statistical relationship between Alfvénic Poynting flux and O<sup>+</sup> ion outflow flux. In the baseline simulation for the 18 April 2002 ICME-driven event, one substorm is observed that is generated by the southward turning of the IMF, after which the magnetosphere-ionosphere system settles into a quasi-steady convection mode. When outflow is included, quasi-periodic substorms are observed suggesting that the sawtooth oscillations are generated internally by the effects of the O<sup>+</sup> ions. In contrast, during the 24 October 2002 SIR-driven event, quasi-periodic substorms are generated regardless of whether outflow is included or not. For this event, the generation and triggering of the substorms is controlled by the external driving of the solar wind. For both events, when outflow is included, the signatures of the substorms are more intense and are more noticeable across a wider range of local times than in the baseline simulations.

**Citation:** Brambles, O. J., W. Lotko, B. Zhang, J. Ouellette, J. Lyon, and M. Wiltberger (2013), The effects of ionospheric outflow on ICME and SIR driven sawtooth events, *J. Geophys. Res. Space Physics*, 118, 6026–6041, doi:10.1002/jgra.50522.

### 1. Introduction

[2] Sawtooth oscillations were first reported by *Borovsky et al.* [1993]. They are so called because the fluxes of energetic charged particles observed at geosynchronous orbit resemble the teeth of a saw blade with a periodic sequence of slow decrease followed by rapid increase [*Belian et al.*, 1995]. During sawtooth events, particle ejections occur quasi-periodically on a timescale of 2–4 h [*Cai and Clauer*, 2009]. Other geophysical processes also vary in sync with the periodic particle injections including magnetic fields in the tail, at geostationary orbit, and on the ground as well as the open flux in the magnetotail and polar cap. In addition, periodic variations are seen in the auroral electrojet,

auroral precipitation, and polar cap indices [*Huang et al.*, 2003; *Kitamura et al.*, 2005; *Cai et al.*, 2006; *Henderson et al.*, 2006; *Huang et al.*, 2009; *Troshichev and Janzhura*, 2009].

[3] The ionospheric and magnetospheric signatures of an individual sawtooth are similar to those of a classic, isolated substorm [*Cai et al.*, 2006] wherein magnetic energy is converted to plasma energy in the Earth’s magnetotail. However, the signatures of sawtooth substorms have a wider local time distribution. The particle injections, dipolarizations, and ground signatures can span from midnight to the dawn-dusk meridian and even onto the dayside. The signatures of sawteeth are also more intense (e.g., the magnetic field is stretched to a greater extent) in the geostationary region than those of isolated substorms.

[4] Sawtooth events are typically identified from the time series of the proton differential energy fluxes captured by geostationary satellites. For a sawtooth event, *Cai and Clauer* [2009] require that observed particle injections are both quasi-global (occurring at multiple magnetic local time (MLT) locations away from local midnight) and quasi-periodic. The requirement for quasi-global signatures eliminates both isolated and periodic substorm events which exhibit particle injections confined to the near midnight

<sup>1</sup>Thayer School of Engineering, Dartmouth College, Hanover, New Hampshire, USA.

<sup>2</sup>Department of Physics and Astronomy, Dartmouth College, Hanover, New Hampshire, USA.

<sup>3</sup>High Altitude Observatory, National Center for Atmospheric Research, Boulder, Colorado, USA.

Corresponding author: O. J. Brambles, Thayer School of Engineering, Dartmouth College, Hanover, NH, USA. (ojbrambles@dartmouth.edu)

region. The requirement of quasi-periodicity further eliminates nonrecurring storm-time substorms that otherwise exhibit particle injections across a wide range of MLT locations similar to sawteeth events.

[5] Two theories have been proposed to explain how sawtooth oscillations are generated: (1) Periodic sawtooth events are related to an intrinsic period of the Earth's magnetosphere and are independent of any external solar wind trigger and (2) sawtooth substorms can be triggered by solar wind discontinuities such as increases in dynamic pressure and fluctuations in the interplanetary magnetic field (IMF) [Huang, 2011]. These differences are not surprising given that sawtooth oscillations have been found to occur during the passage of both Interplanetary Coronal Mass Ejections (ICMEs) and Stream Interaction Regions (SIRs) [Cai and Clauer, 2009; Huang et al., 2004]. During ICMEs, the solar wind conditions are relatively stable, and external triggering by variability in the interplanetary medium is absent or minimal suggesting that the response of the magnetosphere-ionosphere (MI) system is conditioned by an internal mechanism. In contrast, SIRs are characterized by large-scale Alfvénic fluctuations in the interplanetary medium where the direction of IMF  $B_z$  changes direction on a timescale of  $\sim 20$  min to 1 h. It is possible that these periodic solar wind discontinuities provide a recurring trigger which can produce a series of sawtooth substorms.

[6] A relatively steady solar wind with a southward component of the IMF, which is a common condition in the magnetic cloud following the passage of an ICME, may produce both sawtooth oscillations and steady magnetospheric convection (SMC). In contrast to the sawtooth mode of convection, SMC is characterized by enhanced convection without substorm expansion [Sergeev and Lennartsson, 1988] during which the dayside and nightside reconnection rates are approximately balanced [DeJong et al., 2008]. DeJong et al. [2009] studied the upstream solar wind driving for sawtooth oscillations, SMCs, and isolated substorms. The mean velocity during sawtooth oscillations ( $\sim 520$  km/s) is larger than that during SMCs ( $\sim 360$  km/s) and isolated substorms ( $\sim 410$  km/s). The mean IMF  $B_z$  is also more negative during sawtooth oscillations than SMCs or isolated substorms. Sawtooth oscillations occur when IMF  $B_z$  is steady and on average approximately  $\sim -8$  nT. SMCs occur when IMF  $B_z$  is steady and on average  $\sim -3$  nT [O'Brien et al., 2002; McPherron et al., 2008]. In addition, the mean Alfvénic Mach number is smaller during sawtooth events than during SMCs or isolated substorms. Although the average solar wind/interplanetary magnetic field (SW/IMF) conditions that drive sawtooth oscillations and SMCs differ, their variances overlap, indicating that either can occur for similar solar wind and IMF conditions. This behavior suggests that the preconditioning of the MI system is important in determining the mode of convection.

[7] In contrast, intervals of fluctuating IMF almost always produce periodic substorms [Lee et al., 2006]. In addition to the sawtooth oscillations that occur during SIRs, 1–4 h periodic substorms are observed during high-speed streams (HSS). These periodic substorms exhibit signatures consistent with those of classic, isolated substorms [Kamide and Kroehl, 1993; Lee et al., 2006]. Evidently the signatures of these substorms do not display the quasi-global signatures of sawtooth substorms.

[8] Through the use of global simulations of geospace, it has been shown that the outflow of  $O^+$  ionospheric ions into the magnetosphere can generate and trigger sawtooth oscillations for steady solar wind conditions typical of ICMEs [Brambles et al., 2011]. The main mechanism that accelerates  $O^+$  ions and allows them to escape gravity and flow from the ionosphere into the magnetosphere is transverse ion acceleration by wave-particle interactions [Norqvist et al., 1998], followed by mirror force lifting which is directly proportional to the perpendicular ion energy. The first direct observation of energetic (keV), outward flowing ions in the auroral regions ( $64^\circ$  to  $80^\circ$  latitude) was provided by Shelley et al. [1976]. Transverse ion heating and acceleration in the auroral zone was observed by Whalen et al. [1978] and Klumpar [1979]. The heated ions range in energy from tens of electron volts up to several kiloelectron volts [Hultqvist et al., 1991; Yau and André, 1997]. Heavy ion outflows from the ionosphere are most intense in the dayside cusp region [Thelin et al., 1990] and near the polar cap boundary of the nightside auroral zone [Tung et al., 2001; Nosé et al., 2009] where shear Alfvén waves flowing to low-altitude from magnetospheric dynamos deposit electromagnetic power [Keiling et al., 2003; Chaston et al., 2007; Zhang et al., 2012]. A portion of the Alfvén wave energy is converted to ion energy either directly when the transverse scale of the wave becomes comparable to the ion gyroradius [Chaston et al., 2004] or indirectly via secondary instabilities that excite ion gyroscale waves driven by the wave field-aligned current and velocity shear [Seyler and Liu, 2007]. While it is estimated that about 95% of all  $O^+$  outflows are caused by transverse heating associated with low frequency waves [Norqvist et al., 1998], the kinetics of heavy-ion energization are multivariate [Yau and André, 1997; Hultqvist et al., 1999], and a general transport law relating outflow flux to its energy drivers has yet to be determined.

[9] Brambles et al. [2011] showed that as these outflowing  $O^+$  ions fill the inner magnetosphere, their pressure distends the nightside magnetic field from dawn to dusk. The nightside magnetic field is stretched tailward reducing the nightside reconnection rate resulting in the accumulation of open magnetic flux in the tail [Ouellette et al., 2013]. When the open flux in the tail reaches a critical value, which depends upon the strength of solar wind driving [Huang et al., 2009] and the rate and distribution of ionospheric outflow, an instability is generated in the tail which leads to substorm onset [Brambles, 2012]. An  $O^+$ -rich plasmoid is ejected and the magnetic field subsequently dipolarizes. The repetition of the dynamical process is controlled by the intensity of solar wind driving, which regulates the hemispheric outflow rate through electromagnetic energy flows into the ionosphere. For simulations with a hemispheric outflow rate typical of stronger driving conditions, the simulated period is in the range of 2–4 h, consistent with observed sawtooth periods. The simulated sawteeth exhibit the intense and widespread stretching of nightside magnetic field lines, followed by episodic dipolarization that is characteristic of observed sawtooth events. Below a critical threshold, sufficient ion outflow does not accumulate in the plasma sheet to generate the sawtooth mode and the magnetosphere then exhibits steady magnetospheric convection.

[10] The aim of this paper is to determine how ionospheric outflow affects the generation and signatures of periodic substorms for an event driven by an ICME (18 April 2002) and one driven by an SIR (24 October 2002). The study uses a multifluid extension of the Lyon-Fedder Mobarry (LFM) global simulation including a low-altitude boundary condition that allows a causally regulated  $O^+$  fluid to enter the simulation domain. The impact of ionospheric outflow during these events is investigated by comparing a baseline simulation with no outflow to a simulation including ionospheric  $O^+$  outflow. Both events are listed as sawtooth events by *Cai and Clauer* [2009]. Section 2 details the numerical models used in this study, and sections 3 and 4 describe the results for the 18 April 2002 and 24 October 2002 events, respectively. These results are compared and contrasted in section 5.

## 2. Numerical Models

### 2.1. The Lyon-Fedder-Mobarry Global Simulation

[11] The multifluid extension of the Lyon-Fedder-Mobarry (LFM) global simulation code [*Lyon et al.*, 2004] used in this study is based on the following equations:

$$\frac{\partial \rho_\alpha}{\partial t} = -\nabla \cdot (\rho_\alpha \mathbf{u}_\alpha), \quad (1)$$

$$\frac{\partial \mathbf{p}_\alpha}{\partial t} = -\nabla \cdot (\mathbf{p}_\alpha \mathbf{u}_\alpha + \mathbf{I}P_\alpha) + \mathbf{F}_\alpha^d + n_\alpha q_\alpha \mathbf{E}_\parallel, \quad (2)$$

$$\frac{\partial \epsilon_\alpha}{\partial t} = \nabla \cdot \mathbf{u}_\alpha (\epsilon_\alpha + P_\alpha) + \mathbf{u}_\alpha \cdot (\mathbf{F}_\alpha^d + n_\alpha q_\alpha \mathbf{E}_\parallel), \quad (3)$$

$$\frac{\partial \mathbf{B}}{\partial t} = -\nabla \times (\mathbf{u}_M \times \mathbf{B}), \quad (4)$$

where  $\rho_\alpha$ ,  $\mathbf{p}_\alpha$ ,  $\mathbf{u}_\alpha$ ,  $P_\alpha$ , and  $\epsilon_\alpha$  are the species mass density, momentum density ( $\rho_\alpha \mathbf{u}_\alpha$ ), velocity, pressure, and plasma energy ( $\epsilon_\alpha = \frac{1}{2} \rho_\alpha \mathbf{u}_\alpha^2 + \frac{P_\alpha}{\gamma-1}$ ), respectively.  $\mathbf{u}_M$  is the center of mass velocity and in the perpendicular direction is the same for all species. The subscripts  $\alpha$  (along with  $\beta$  in equation (5) below) represent the individual ion species. The local magnetic field is given by  $\mathbf{B}$ , while  $n_\alpha$  and  $q_\alpha$  are the ion species number density and charge, respectively. The ambipolar electric field is  $\mathbf{E}_\parallel = \hat{\mathbf{b}} \hat{\mathbf{b}} \cdot \nabla P_e / ne$  where  $P_e$  is the electron pressure and  $n = \sum n_\alpha$  is the electron density.  $\mathbf{F}_\alpha^d$  is the Lorentz force due to the first order (in  $1/(\Omega_\alpha \tau)$ ) ion drift given by

$$\mathbf{F}_\alpha^d = \hat{\mathbf{b}} \times \left[ \mathbf{p}_\alpha \cdot \nabla \mathbf{u}_\alpha + \nabla P_\alpha + \frac{\rho_\alpha (\mathbf{u}_M - \mathbf{u}_\alpha) \cdot \hat{\mathbf{b}}}{\mathbf{B}} \frac{\partial \mathbf{B}}{\partial t} - \frac{\rho_\alpha}{\rho} \left( \sum_\beta (\mathbf{p}_\beta \cdot \nabla \mathbf{u}_\beta + \nabla P_\beta) + \nabla P_e - \mathbf{j} \times \mathbf{B} \right) \right] \times \hat{\mathbf{b}}. \quad (5)$$

Here  $\hat{\mathbf{b}} = \mathbf{B}/B$ ,  $\Omega_\alpha$  is the ion species gyrofrequency, and  $\tau$  is the magnetohydrodynamic MHD timescale. In the simulation, the two ion species drift at the  $\mathbf{E} \times \mathbf{B}$  velocity perpendicular to the ambient magnetic field. The flow parallel to  $\mathbf{B}$  of the two species is coupled via the parallel electric field. Within the model, the electron pressure is specified as a fraction of the total ion pressure and is locally partitioned between the ion species based on the relative ion species

charge fractions. In this paper, it is assumed that the electrons are a cold neutralizing fluid with zero temperature and pressure which facilitates understanding the system in a simpler limit. Further discussion regarding this limit is given by *Brambles et al.* [2010].

[12] The model equations are solved on a nonuniform, nonorthogonal grid (which gives higher resolution in the near-Earth and bow shock regions) that stretches from 30  $R_E$  upstream to 300  $R_E$  downstream with the cylindrical extent of the simulation domain extending to a radius of 100  $R_E$ . The grid resolution ranges from 0.25 to 0.50  $R_E$  in the inner magnetosphere and bow shock, increasing to 1 to 2  $R_E$  in the region of nightside reconnection and to approximately 15 to 20  $R_E$  at distances greater than 100  $R_E$ . The inner boundary of the LFM magnetosphere domain is a sphere with a radius of 2  $R_E$ . Below this altitude, collisionless microphysics are important in describing the dynamics of the plasma and the ideal MHD equations are no longer valid.

[13] An electric field and convection velocity are imposed on the plasma fluid at the low-altitude boundary grid cell. Their values are determined by introducing a simple, height-integrated model for the interaction between the magnetosphere and the ionosphere. The ionosphere model solves for the electric potential,  $\Psi$ , using the height-integrated model for the ionospheric conductance tensor  $\bar{\Sigma}$ . When Ohm's law in the ionosphere is combined with current continuity and given that the field-aligned conductance is much greater than the Pedersen and Hall conductances, the ionosphere model has the form

$$\nabla \cdot \bar{\Sigma} \cdot \nabla \Psi = j_\parallel \sin \delta \quad (6)$$

where  $j_\parallel$  is the field-aligned current mapped to the ionosphere from the low-altitude simulation boundary, and  $\delta$  is the magnetic dip angle. The Pedersen and Hall conductances in  $\bar{\Sigma}$  are calculated using empirical models for both the EUV-induced and precipitation-induced conductance. The EUV-induced contributions are parameterized by the  $F_{10.7}$  flux and the solar zenith angle. The precipitation-induced contributions use the *Robinson et al.* [1987] formulas with precipitating electron energy and energy flux derived from the MHD variables at the low-altitude boundary of the simulation [*Fedder et al.*, 1995; *Wiltberger et al.*, 2009]. The electric potential obtained from equation (6) is then mapped upward along dipole magnetic field lines to the inner boundary where the electric field,  $\mathbf{E}$ , and corresponding  $\mathbf{E} \times \mathbf{B}$  convection velocity are calculated and imposed as boundary conditions on the MHD equations.

### 2.2. Outflow Model

[14] The outflow model utilizes an observed statistical correlation between Alfvénic Poynting flux and an accelerated  $O^+$  outflow flux as described in the supplementary material of *Brambles et al.* [2011].  $H^+$  (proton) outflow is not included in this study in order to focus solely upon the effects of transversely accelerated  $O^+$  ions on the dynamics of magnetospheric convection. It will be important in future studies to assess the relative importance of ionospheric  $H^+$  and  $O^+$  ion outflow on the magnetosphere. The outflow flux is given by the equation

$$F_{O^+} = 2.97 \times 10^{10} \alpha S_\parallel^{1.2}, \quad (7)$$

where  $F_{O^+}$  is the outflow flux in ions/cm<sup>2</sup>-s,  $\alpha$  is a scaling constant and  $S_{\parallel}$  is the Alfvénic Poynting flux in mW/m<sup>2</sup>:

$$S_{\parallel} = \left\langle \frac{\delta \mathbf{E} \times \delta \mathbf{B} \cdot \mathbf{B}}{|\mathbf{B}| \mu_0} \right\rangle_{1\text{min}}. \quad (8)$$

Here  $\delta \mathbf{E}$  and  $\delta \mathbf{B}$  are the deviations of the electric and magnetic fields  $\mathbf{E}$  and  $\mathbf{B}$  from their 3 min running averages. The resulting Poynting flux is then averaged over 1 min to remove the standing wave component. Although the statistical correlation relation (7) exhibits considerable variance in observations and alone does not establish a direct causal link between  $F_{O^+}$  and  $S_{\parallel}$ , it does provide an empirical means of specifying an average outflow flux at the low-altitude simulation boundary for a given Poynting flux flowing downward through the boundary. Given the statistical uncertainties in equation (7) and in the correspondence between satellite measurements and MHD simulations of Alfvénic Poynting, a variable scaling factor  $\alpha$  has been introduced. An  $\alpha$  of 3.8 is used in this study which was chosen based upon the results from the study by *Brambles et al.* [2011]. For this value of  $\alpha$ , the simulated hemispheric outflow rate is consistent with reported estimated values based on statistics of observed outflows [*Yau and André, 1997*].

[15] The MHD code requires boundary conditions on the density, velocity, and temperature for each fluid. The outflow flux is related to density and velocity by the equation  $F_{O^+} = n_{O^+} v_{\parallel O^+}$  where  $n_{O^+}$  is the outflow number density and  $v_{\parallel O^+}$  is the field-aligned velocity of the outflowing fluid at the boundary. In these simulations, the velocity is specified to be constant in space and time. This assumption is based upon the study by *Bouhram et al.* [2004], which found that the greatest variability in observed  $O^+$  outflow at 2.3  $R_E$  geocentric is due to variations in the density. With a constant, specified velocity, the density can be calculated as  $n_{O^+} = F_{O^+}/v_{\parallel}$ . To be consistent with the results shown in *Bouhram et al.* [2004, Figure 4] for transversely accelerated outflow at 2  $R_E$  geocentric, the parallel velocity is specified to be 45 km/s.

[16] The MHD code also requires a specification of the ion temperature. The processes that regulate the ion temperature are not well understood. Statistical studies suggest that outflow temperature varies with longitude and latitude [*Peterson et al., 2008*], however, in this simulation the outflow temperature is simply specified as being constant in space and time. To be consistent with *Bouhram et al.* [2004, Figure 4], the temperature is set to be 100 eV at inner boundary of the simulation. It should also be noted that in the simulation, the temperature is isotropic whilst in reality, the outflow temperature is highly anisotropic.

### 3. 18 April 2002 Sawtooth Event

[17] The geomagnetic storm on 18 April 2002 was generated by a magnetic cloud that was part of a sequence of interplanetary coronal mass ejections that impacted geospace between 17 and 24 April. Figure 1 shows the IMF and solar wind plasma data that were used to drive the global simulation. The simulation began at 2000 UT on 17 April in order to precondition the magnetosphere before the ICME arrived. The 1 min data samples in the figure were obtained from OMNI data set at [http://cdaweb.gsfc.nasa.gov/istp\\_public](http://cdaweb.gsfc.nasa.gov/istp_public), and were ballistically propagated to the upstream boundary

of the multifluid Lyon-Fedder-Mobarry (MFLFM) simulation at 30  $R_E$  using  $v_x$  from the solar wind data. In solar magnetic (SM) coordinates, the  $z$  axis is parallel to the north magnetic pole and the  $y$  axis is perpendicular to the Earth-Sun line toward dusk. Assuming no variation in  $v_{SM}$  or  $z_{SM}$  of the upstream variables, the solar wind density, velocity, and sound speed and the IMF  $B_y$  and  $B_z$  are used as upstream boundary conditions to drive the simulation. At the upstream boundary, the tilt in IMF direction relative to the solar wind velocity (while maintaining  $\nabla \cdot \mathbf{B} = 0$ ) is approximately accounted for by specifying the  $B_x$  component as a linear combination of  $B_y$  and  $B_z$ , ( $B_x(t) = B_{x,0} + cB_y(t) + dB_z(t)$ ).  $B_{x,0}$ ,  $c$ , and  $d$  are constants derived by least squares fitting to the observed solar wind time series [*Lyon et al., 2004; Goodrich et al., 2007*]. Dipole tilt is accommodated by inputting the solar wind in solar magnetic (SM) coordinates. As the dipole axis rotates throughout the day, the apparent solar wind direction is changed up and down in the SM-Z direction [*Lyon et al., 2004*].

[18] The solar wind is characterized by a sudden increase in the intensity of the plasma density (also dynamic pressure) and a change from northward to southward IMF in the early hours of 18 April 2002. The solar wind shows little variation after 0400 UT. The solar wind has a low density, a relatively steady velocity, and a southward IMF  $B_z$ . The storm is classified as moderate with a minimum Dst of  $-130$  nT. Despite these relatively steady solar wind conditions, the flux profiles of the LANL/SOPA geosynchronous energetic electron and proton measurements captured quasi-periodic particle injections. The particle injections had a period of 2–3 h and exhibited the characteristic sawtooth signatures [*Henderson et al., 2006*].

[19] The 18 April 2002 sawtooth event has been previously simulated using the single fluid version of the LFM global simulation [*Goodrich et al., 2007*]. The simulation captured several dipolarizations which were significantly smaller in scale than observed. The convection in the magnetotail was characterized by intermittent bursts of flow, produced from patchy reconnection in the midtail. While most of these flows are diverted to the flanks to produce the general convection pattern, some of these flows periodically reach the inner magnetosphere and cause localized plasma injections and field dipolarizations. The simulation was unable to capture the large scale, 2–3 h global periodic loading and unloading of the magnetosphere. The baseline simulation gives results similar to the *Goodrich et al.* [2007] study. The results will not be identical owing to differences between the single fluid version of the model used by *Goodrich et al.* [2007] and multifluid version used in this study. The difference between these results is mainly manifested in the smaller-scale variability such as the timings and magnitude of bursty tail reconnection.

#### 3.1. Outflow Characteristics

[20] Figure 2 shows the  $O^+$  hemispheric outflow rate emerging from the (top) northern and southern ionospheres, IMF  $B_z$  (Figure 2, middle) and the solar wind dynamic pressure (Figure 2, bottom) located at the upstream boundary of the MFLFM global simulation. The hemispheric outflow rate is calculated at 3  $R_E$  geocentric distance and mapped along dipole field lines to an ionospheric altitude of 100 km. The hemispheric outflow rate exhibits

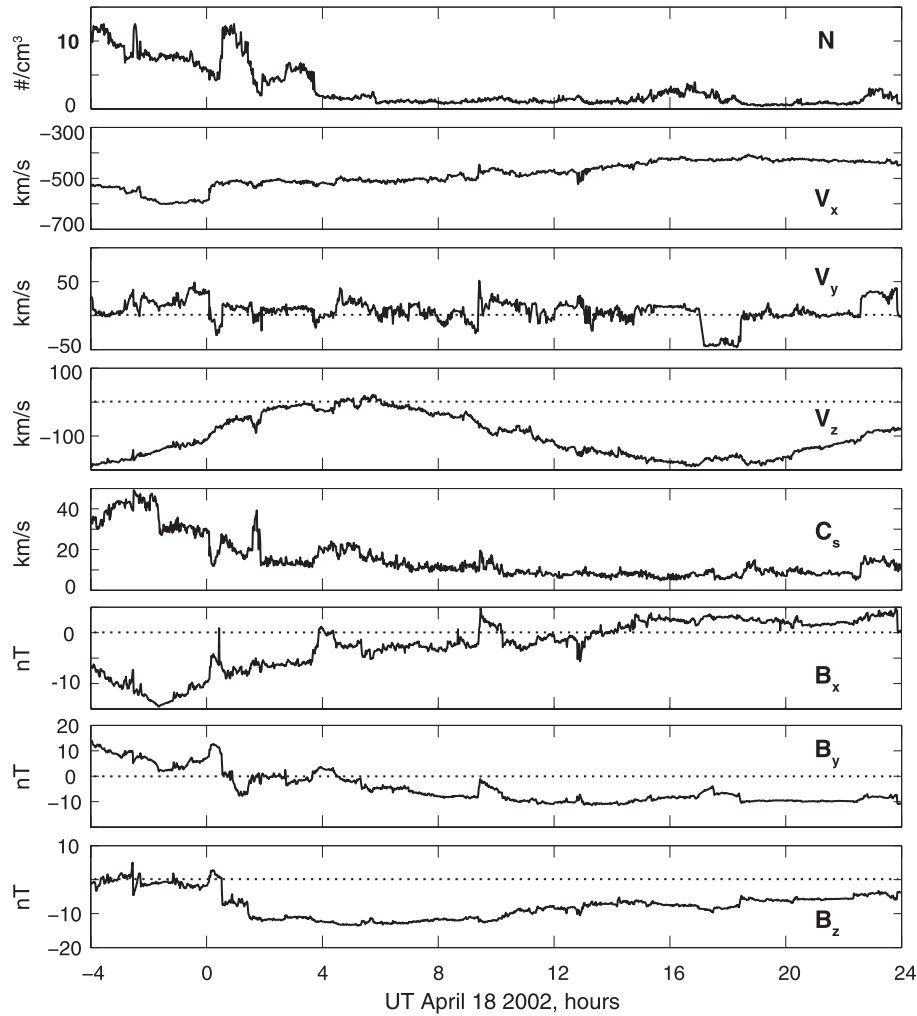


**Figure 1.** Solar wind parameters for the 18 April 2002 storm used as upstream boundary condition in LFM simulation. (top to bottom) Plasma density, velocity components, sound speed, and interplanetary magnetic field components in SM coordinates.

quasi-periodic behavior that is not correlated with changes in the solar wind parameters. This variability is associated with the electromagnetic power generated by dipolarizations in the inner magnetosphere. The hemispheric outflow rate is highest between 0200 UT and 0400 UT when the dynamic pressure is the highest and IMF  $B_z$  is most negative. The hemispheric outflow rate from the northern, summer hemisphere is generally higher than that from the southern, winter hemisphere. The average hemispheric outflow rate in the northern hemisphere is  $2.6 \times 10^{26}$   $O^+$  ions/s compared to  $2.1 \times 10^{26}$   $O^+$  ions/s in the southern hemisphere. This result is consistent with the statistical observations by *Lennartsson et al.* [2004] and with simulated results from the study by *Brambles et al.* [2010] who used an outflow model regulated by the low frequency components of Poynting flux (DC Poynting flux) during the 31 August 2005 storm. (In contrast, the Alfvénic Poynting flux used, in *Brambles et al.* [2011] and in this study, is separated from these lower frequency components by using a bandpass filter of 5–180 s. For more information, see supplementary material of [*Brambles et al.*, 2011]). The exact mechanisms that cause the hemispheric outflow rate and Alfvénic power to be

higher in the summer hemisphere are not known. *Brambles et al.* [2010] determined that the higher Pedersen conductance induced by a higher EUV flux in the summer hemisphere causes the DC Poynting (and outflow) flux to be larger. In April, the Northern hemisphere has a higher incidence of EUV flux than the Southern hemisphere, which suggests that the hemispheric outflow rate should be higher in the Northern hemisphere. It is possible that in the simulation shown here, an increase in DC Poynting flux and overall power flowing into the summer hemisphere will also result in an increase in Alfvénic power. For example, the field-aligned currents flowing into the ionosphere in the simulation are approximately 33% higher in the northern hemisphere than in the southern hemisphere.

[21] The morphology of the average outflow flux for the day of 18 April is shown in Figure 3. Hourly averages exhibit patterns similar to the daily average due to the relatively steady solar wind conditions. The outflow is located throughout the auroral oval on both the dayside and nightside with peaks in both premidnight and postmidnight sectors at approximately  $65^\circ$  magnetic latitude (MLAT), and in prenoon and postnoon sectors at approximately

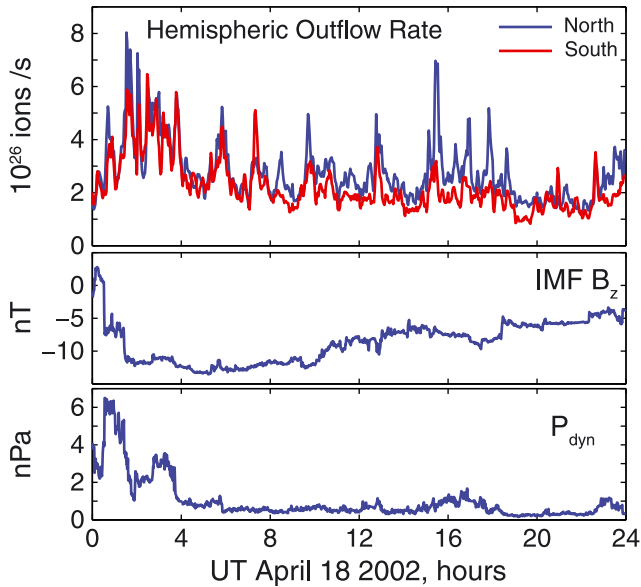


**Figure 2.** The 18 April 2002 storm characteristics. (top)  $O^+$  hemispheric outflow rate in the northern and southern hemispheres, (middle) IMF  $B_z$ , and (bottom) solar wind dynamic pressure.

$69^\circ$  MLAT. The nightside morphology is consistent with statistical maps of Alfvénic Poynting flux [Keiling *et al.*, 2003] and outflow flux [Dang *et al.*, 2007; Lennartsson *et al.*, 2004]. The outflow flux is approximately 15% higher on the dusk side than on the dawn side, which is also a feature of the results reported by Brambles *et al.* [2011]. This difference arises due to the asymmetry in the Alfvénic power which is caused by the precipitation-induced ionospheric conductance [Zhang *et al.*, 2012]. The simulation produces significant outflow flux in the cusp in the northern hemisphere ( $\approx 2 \times 10^9$  ions/cm<sup>2</sup>-s), located at approximately 1200 MLT at  $70^\circ$  MLAT, but the outflow flux in the southern hemisphere is considerably lower ( $\approx 4 \times 10^8$  ions/cm<sup>2</sup>-s). This difference is possibly caused by the asymmetry of the solar wind impinging on the Earth which results from the simulated dipole tilt angle and direction of the solar wind or due to the relative differences in the EUV-induced ionosphere conductance. Due to the relatively steady solar wind conditions, the outflow in the cusp is lower than in the dayside auroral region (either side of noon at 0900 and 1500 MLT) in both hemispheres. In this simulation MHD activity is enhanced in the vicinity of the flankside magnetopause. This activity is likely due to Kelvin-Helmholtz waves which increase in amplitude away from the subsolar magnetopause. This effect may explain the paucity of Alfvénic power flowing into the cusp relative to the dayside auroral region. Intense hemispheric outflow rates are evident in the Northern hemisphere at approximately  $62^\circ$  MLAT at 1200 MLT. Since Figure 3 shows a daily average of the outflow, this low-latitude feature is most likely due to discontinuities that appear in the SW/IMF in Figure 1.

### 3.2. Results

[22] The 18 April 2002 storm produced a sequence of seven substorms (see Table 1 for timings), which were

observed in a wide range of geophysical parameters. The comparison between observed and simulated data is restricted to geophysical processes that can be derived from the magnetohydrodynamic equations in the LFM simulation. In this study, a combination of the open magnetic flux in the lobes and polar cap, and magnetic fields in the inner magnetosphere and magnetotail will form the basis of the comparison.

[23] Figure 4, top shows the polar cap and magnetotail (Figure 4, bottom) magnetic flux inferred from observations and from baseline and outflow simulations. The observed polar cap magnetic flux was calculated by Huang *et al.* [2009] using data from the Far Ultraviolet (FUV) Imager on board the Polar satellite. The simulated open magnetic flux in the polar cap is evaluated by first tracing magnetic field lines to determine the location of the separatrix distinguishing open from closed field lines. This separatrix is then mapped to the ionosphere and the magnetic flux through the enclosed surface is calculated. The calculation of the observed open magnetic flux in the magnetotail uses plasma

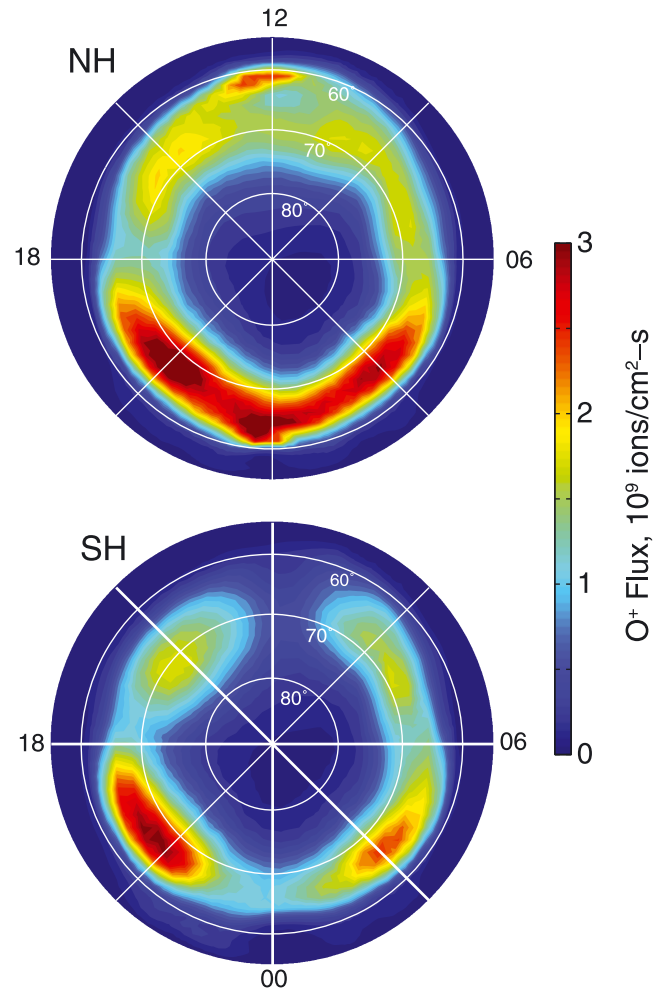


**Figure 3.** Daily average of the outflow flux mapped to a reference altitude of 100 km in (top) northern hemisphere and (bottom) southern hemisphere during 18 April 2002 sawtooth event. Positional coordinates are given by magnetic latitude and magnitude local time.

**Table 1.** Onset Times for the 18 April 2002 Sawtooth Event From Observations [Cai and Clauer, 2009], Baseline Simulation and Outflow Simulation<sup>a</sup>

Sawtooth Number	Observed Onset (UT)	Baseline Onset (UT)	Outflow Onset (UT)	Outflow UT — Observed UT (h)	Is Outflow Required?
1	0237	0156	0215	-0:22	no
2	0529		0652	+1:23	yes
3	0755		0920	+1:25	yes
4	1130		1302	+1:32	yes
5	1405		1520	+1:15	yes
6	1630	1810	1812	+1:42	unknown
7	2103		2230/2318	+1:27/2:15	yes

<sup>a</sup>Onset times for baseline and outflow simulations are calculated using a combination of the open magnetic flux in the polar cap and the magnetic fields at 9 R<sub>E</sub> in the nightside magnetosphere.

and field data taken from Geotail [Huang *et al.*, 2009]. The open magnetic flux in the magnetotail is defined as  $F_T = \pi R_T^2 B_L/2$ .  $R_T$  is the tail radius at the location of the Geotail satellite and is calculated using an empirical model [Shue *et al.*, 1997].  $B_L$  is the equivalent lobe magnetic field calculated as  $B_L^2/2\mu_0 = B_T^2/2\mu_0 + N_i k(T_i + T_e)$  where  $B_T = (B_x^2 + B_y^2 + B_z^2)^{1/2}$  and  $N_i k(T_i + T_e)$  is the plasma thermal pressure. The magnetic pressure is much greater than the plasma pressure in the tail lobes while the plasma pressure dominates the magnetic pressure in the plasma sheet. The calculation of the equivalent lobe magnetic field assumes that in the plasma sheet, the lobe magnetic pressure is balanced by the plasma sheet plasma pressure. This assumption is based upon studies that show that the lobe and plasma sheet are in pressure balance both instantaneously and statistically [Baumjohann *et al.*, 1990; Spence *et al.*, 1989; Huang and Cai, 2009]. The calculation of the magnetotail flux is a product of the magnetotail cross section ( $\pi R_T^2/2$ ) that includes a tail lobe and half the plasma sheet and the equivalent lobe magnetic field  $B_L$ . It is assumed in this calculation that the equivalent lobe magnetic field measured by Geotail is the average over the semicircular magnetotail cross section. For the purposes of comparison, in the simulation the equivalent lobe magnetic field is calculated using the same method. The simulation allows for a more direct calculation of the tail radius. The empirical model of Shue *et al.* [1997] does not capture the expansion and contraction of the tail radius over a substorm cycle. In the simulation, the tail radius is estimated as being half the distance between the flanks of the magnetopause at the radial distance of Geotail.

[24] The open magnetic flux in the outflow simulation shown in Figure 4 exhibits sawtooth-like characteristics with a period of 2–4 h. In observed data, both isolated and sawtooth substorms are characterized by an increase of open magnetic flux during the growth period, followed by a rapid decrease during the expansion phase [Huang *et al.*, 2009]. However, the mean open magnetic flux at onset is larger for a sawtooth substorm (1.04 GWb) than for an isolated substorm (0.67 GWb) [Huang *et al.*, 2009]. The magnetic flux variation in the outflow simulation exhibits a different phasing compared with observed flux variations, but the general cycle of loading and unloading and approximate period is common to both. In contrast, the polar cap flux in the baseline simulation shows one cycle of loading and unloading and then is relatively steady from 0200 UT to 1600 UT. The baseline simulation displays variability in the magnetic flux

on time scales of approximately 30 min to 1 h, which are produced by bursty tail reconnection as discussed by Goodrich *et al.* [2007]. The red vertical lines in Figure 4 correspond to the onset of large decreases in the open magnetic flux in the polar cap for the outflow simulation. The black vertical lines delineate the onset times identified by Cai and Clauer [2009] based on particle injections at geostationary orbit. The times of the onsets for the observed, baseline, and outflow simulation are given in Table 1.

[25] Ionospheric outflow is not required to generate the first substorm. The onset for the baseline simulation at 0156 UT is earlier than for the outflow simulation (0216 UT). This

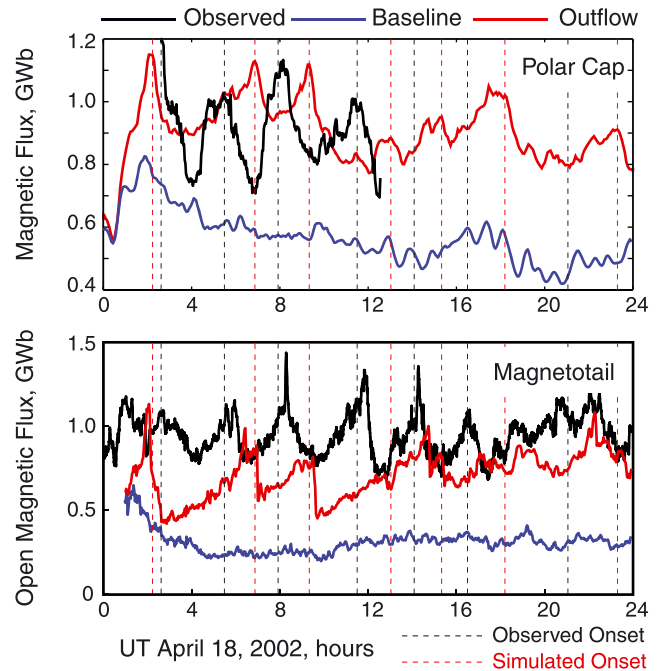


**Figure 4.** Magnetic flux derived from observations (black) taken from Huang *et al.* [2009], baseline simulation (blue), and outflow simulation (red) calculated at the (top) polar cap and (bottom) magnetotail during 18 April 2002 sawtooth event. Red vertical dashed lines show substorm onsets in the outflow simulation. Black vertical dashed lines show observed substorm onsets reported by Cai and Clauer [2009].

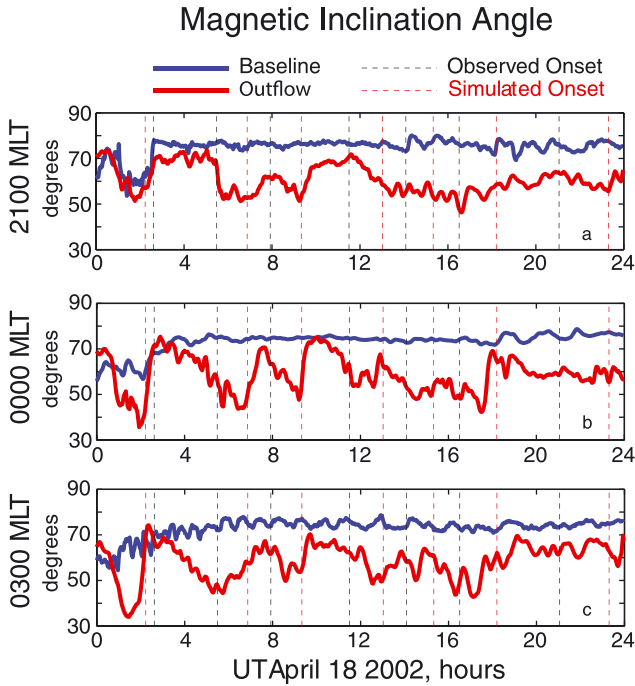


**Figure 5.** Magnetic inclination angle calculated at  $9 R_E$  in the SM equatorial plane at (top) 2100 UT, (middle) 0000 UT, and (bottom) 0300 MLT for the baseline simulation (blue) and outflow simulation (red) during 18 April 2002 sawtooth event. Red vertical dashed lines show substorm onsets calculated using the open magnetic flux in the outflow simulation. Black vertical dashed lines show observed substorm onsets reported by *Cai and Clauer* [2009].

result is consistent with *Wiltberger et al.* [2010] who found that the influence of ionospheric outflow in the plasma sheet delayed substorm onset. The first onset observed in satellite data was at 0237 UT. It is possible that in the simulation, onset is caused by the jump in solar wind dynamic pressure (see Figure 2c) at 0200 UT, and the actual system is triggered by the increase at 0238 UT. The peak in the polar cap magnetic flux is larger in the outflow simulation (1.1 GWb) than in the baseline simulation (0.8 GWb). The outflow simulation then settles into a sequence of sawtooth oscillations with four onsets at 0652 UT, 0920 UT, 1302 UT, and 1520 UT seen in both the polar cap and magnetotail magnetic flux. During this time the baseline simulation shows no obvious substorm signatures. The timing of each of the substorms in the outflow simulation is approximately 1 h 20 min later than the equivalent observed substorm. The onset of the second substorm is delayed in the simulation relative to the observed onset, but the period of the subsequent substorms (2.75 h) is similar. Between 0000 UT and 1600 UT, the magnetic flux time series at the polar cap and in the magnetotail show similar profiles. However, after 1600 UT, the profiles begin to diverge. In the outflow simulation, decreases in open magnetic flux in the polar cap are observed at 1812 UT and 2318 UT. In contrast, in the magnetotail, a single decrease in open flux is observed at 2230 UT. This divergence may be due to the location of the Geotail satellite relative to the position of nightside reconnection in the simulation. The satellite moves from  $x = -20 R_E$  GSM to  $x = -30 R_E$

GSM throughout the course of the day. In the geocentric solar magnetospheric (GSM) coordinate system, the  $x$  axis is coincident with the direction of the Sun and the XZ plane contains the dipole axis. The polar cap magnetic flux suggests that there may be a substorm in both the baseline and outflow simulations at approximately 1812 UT. In the outflow simulation, a final plasmoid is ejected at approximately 2245 UT, observed from an animation of the nightside field lines, which causes a series of dipolarizations in the inner magnetosphere. These dipolarizations are observed in the magnetotail flux at approximately 2230 UT and in the polar cap flux at 2317 UT.

[26] Figure 5 shows the magnetic inclination angle at three locations (2100 MLT, 0000 MLT, and 0300 MLT) at a radius of  $9 R_E$  in the SM equatorial plane (i.e., the plane perpendicular to the magnetic dipole axis) for the baseline and outflow simulations. The features discussed herein also appear at  $6.6 R_E$  as analyzed by *Brambles et al.* [2011] but are even more pronounced at  $9 R_E$ . It should be noted that due to asymmetry in the structure of the tail resulting from the effects of the tilt angle and direction of the solar wind, 0000 MLT will not necessarily be at the center of the plasma sheet. The time series of the magnetic inclination angle captures the stretching and dipolarization of the field lines for the first substorm in both the baseline and outflow simulation. In the baseline simulation, the field dipolarization is most apparent at 0000 and 2100 MLT with a small

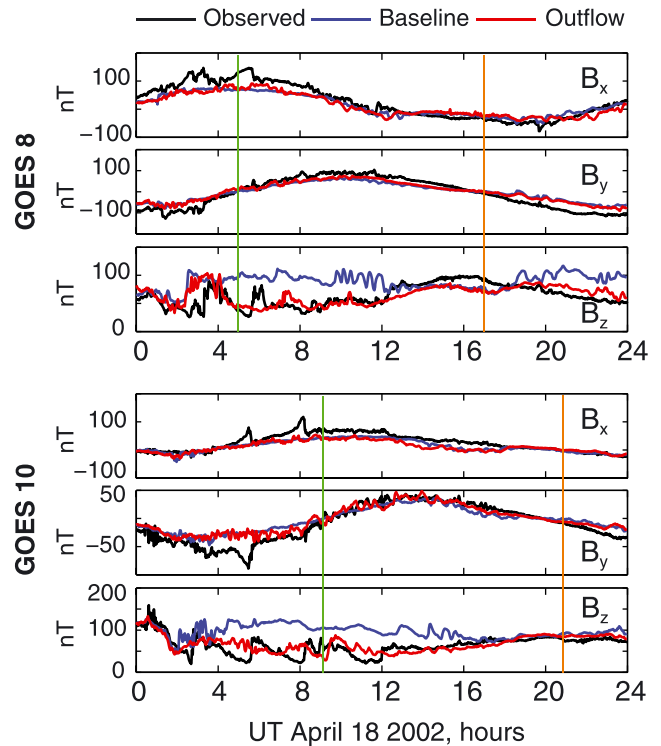


**Figure 6.** Comparison of magnetic field taken at GOES 8 and 10 (black) with simulated magnetic fields at GOES 8 and 10 for baseline (blue) and outflow (red) simulations during 18 April 2002 sawtooth event. Vertical green and orange denote the times when the satellite passed through GSM midnight and noon, respectively.

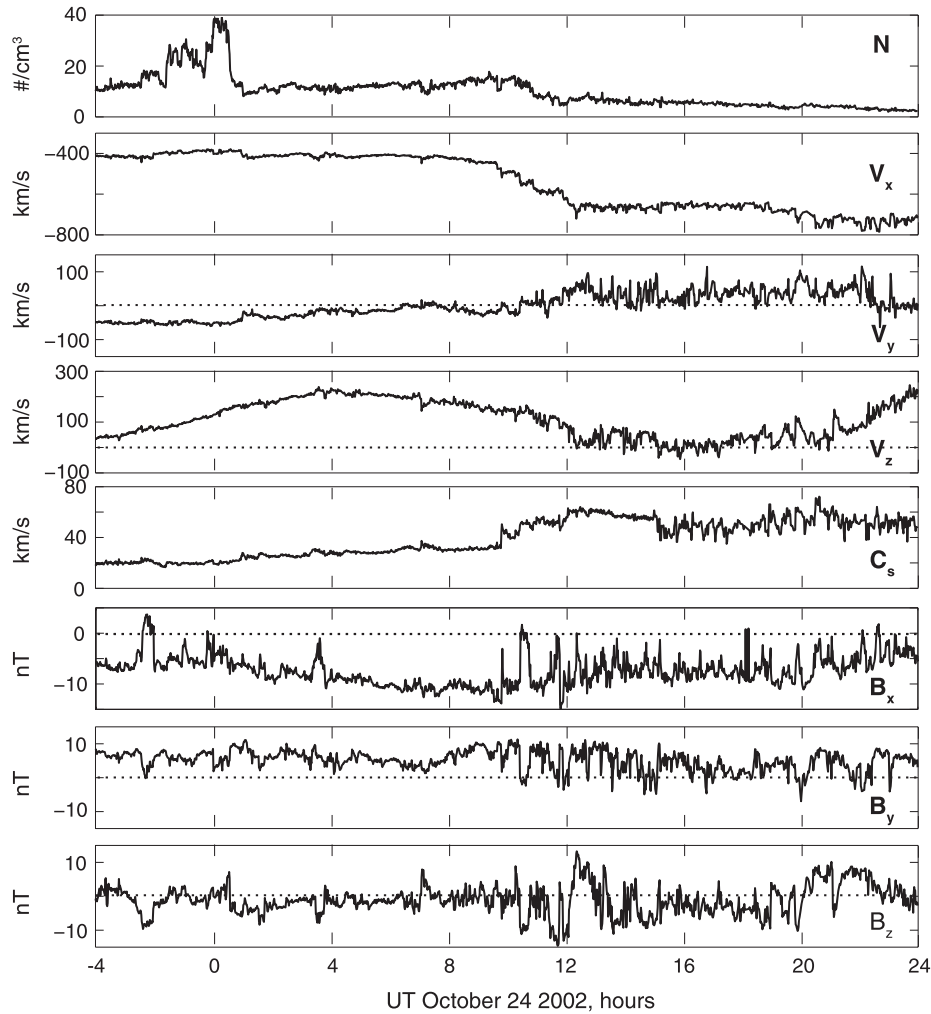


**Figure 7.** Solar wind parameters for the 24 October 2002 storm used as upstream boundary condition in the LFM simulation. Same format as Figure 1.

dipolarization at 0300 MLT. In the outflow simulations, the dipolarization covers a wider range of MLT and is more intense. At 0300 UT, the magnetic inclination has a minimum of  $35^\circ$  in the outflow simulation, but only  $60^\circ$  in the baseline simulation.

[27] This additional stretching originates from the increased number of  $O^+$  ions that accumulate in the plasma sheet and ring current during both the preconditioning time and during the growth phase. This  $O^+$  population enhances both the “ballooning” pressure force and the diamagnetic ring current that shears the ambient magnetic field. Both effects act to distend and stress the magnetic field lines [Brambles *et al.*, 2011]. Analysis by Ouellette *et al.* [2013] also suggests that the inflation of the tail is a response to the increased mass-loading of the plasma sheet by the  $O^+$  ions. Additional diagnostics are required to determine which of these effects is dominant. This stretching has also been observed in the BATS-R-US global simulation when ionospheric outflow is included [Glocer *et al.*, 2009a].

[28] After the first substorm, the time series of the inclination angle for the baseline simulation shows little variation, suggesting that the magnetosphere enters a period of quasi-steady convection. No dipolarization is found in the baseline

simulation at 1810 UT indicating that the change in polar cap open flux was simply due to variability and not the signatures of a substorm.

[29] In contrast, the magnetic inclination in the outflow simulation at 0000 MLT shows periodic field line stretching and dipolarizations, the timings of which are generally consistent with the oscillations in magnetic flux. The inclination angle at 0300 MLT and 2100 MLT exhibit some of the substorm onsets, but not all. Some of the onsets could be weaker because the SM equatorial plane may be offset from the center of the plasma sheet due to the effect of the varying dipole tilt angle and asymmetric solar wind driving. In addition, the outflow introduces additional variability [Garcia *et al.*, 2010] that may mask the dipolarizations further away from midnight.

[30] Figure 6 shows a comparison of the magnetic field line measured at the GOES 8 and GOES 10 satellites with the field derived from the outflow baseline and outflow simulations. The simulation with outflow shows a large improvement in  $B_z$  measured at both GOES 8 and 10, consistent with the results from Glocer *et al.* [2009a, 2009b]. The enhanced reduction in  $B_z$  when outflow is included causes a reduction in the magnetic inclination angle. Evidence of the

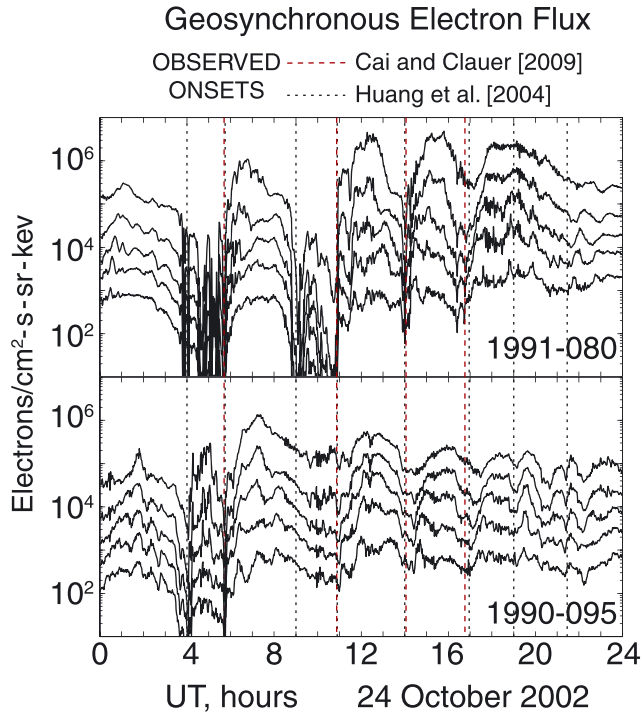


**Figure 8.** Electron fluxes from geostationary satellites from LANL satellites (top) 1991-080 and (bottom) 1990-095 taken from *Huang et al.* [2004] during the 24 October 2002 event. Black vertical dashed lines indicate nightside activity (substorm onset) calculated by *Huang et al.* [2004] and red vertical dashed lines indicate sawtooth onset calculated by *Cai and Clauer* [2009].

sawtooth substorms can be seen in both  $B_x$  and  $B_z$  on the GOES 8 and 10 satellites. However, this periodicity can only be easily observed in  $B_z$  for the simulated event with outflow. Increased variability is found in  $B_x$  in the outflow simulation compared to the baseline simulation, but the magnitude is small compared to the observed  $B_x$ . The resolution in the inner magnetosphere may affect the comparison between simulated and magnetic fields at GOES.

#### 4. The 24 October 2002 Sawtooth Event

[31] The geomagnetic storm on 24 October 2002 was generated by a stream interaction region (SIR). The minimum Dst for this storm was  $-98$  nT and was a weaker storm than the ICME-driven event on 18 April 2002. The 1 min data samples in the figure were obtained from OMNI data set at [http://cdaweb.gsfc.nasa.gov/istp\\_public](http://cdaweb.gsfc.nasa.gov/istp_public), and were ballistically propagated to the upstream boundary of the MFLFM simulation at  $30 R_E$  using  $v_x$  from the solar wind data. Figure 7 shows the IMF and solar wind plasma data that were used to drive the simulation. The simulation was started at 2000 UT on 23 October in order to precondition the magnetosphere-ionosphere system. The IMF fluctuated between southward and northward throughout the day on 24 October on a timescale of approximately 15 min to 1 h. Before 1000 UT on 24 October, the peak magnitude of the oscillating IMF was approximately 5 nT, after which it

increased to over 10 nT. Before 1000 UT, the solar wind velocity  $v_x$  did not show significant variability and was on average 460 km/s. Between 1000 UT and 1200 UT, the solar wind velocity increased to 670 km/s and then remained relatively steady for the remainder of the day.

[32] Electron fluxes measured by the LANL 1991-080 and 1990-095 satellites showed periodic flux injections occurring at multiple local times away from local noon, consistent with sawtooth substorms [*Huang et al.*, 2004] (Figure 8). *Huang et al.* [2004] determined that there were eight particle injections which may have been associated with substorms between 0400 UT and 2124 UT with a period of approximately 2:30 h. Apparently, not all of these injections satisfied the quasi-global requirement by *Cai and Clauer* [2009] who determined that there was a sequence of only four sawteeth occurring between 0542 UT and 1638 UT. The red vertical dashed lines in Figure 8 indicate the timings of particle injections determined by *Cai and Clauer* [2009], and the black vertical dashed lines indicate the onset of each tooth determined by *Huang et al.* [2004]. Previous analysis suggests that the substorm onsets were not all triggered by discontinuities in the solar wind (e.g., a large northward turning of the IMF) [*Huang et al.*, 2004].

#### 4.1. Outflow Characteristics

[33] Figure 9 shows the  $O^+$  hemispheric outflow rate in the northern and southern hemispheres (Figure 9, top), IMF  $B_z$  (Figure 9, middle) and the solar wind dynamic pressure (Figure 9, bottom) located at the upstream boundary of the simulation. The hemispheric outflow rate is larger when the peak magnitude of the oscillating IMF and solar wind velocity are larger and is largest at approximately 1300 UT when the IMF rapidly changes from southward to northward IMF.

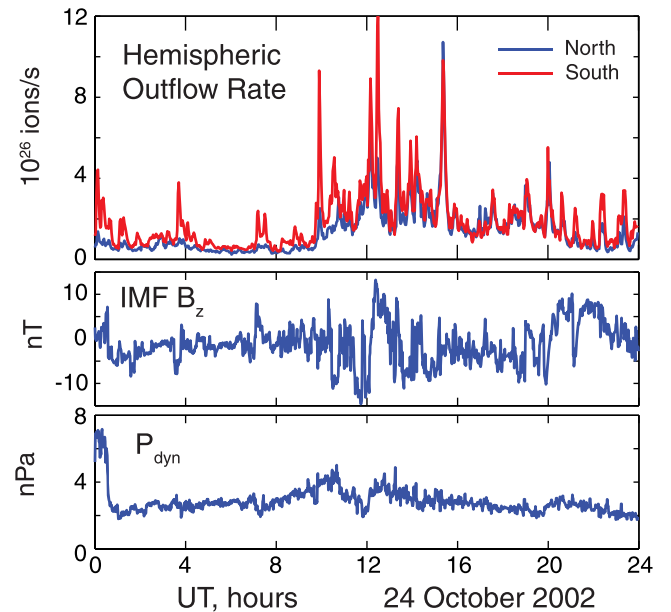


**Figure 9.** The 24 October 2002 SIR storm characteristics. (top)  $O^+$  hemispheric outflow rate in the northern and southern hemispheres, (middle) IMF  $B_z$ , and (bottom) solar wind dynamic pressure.

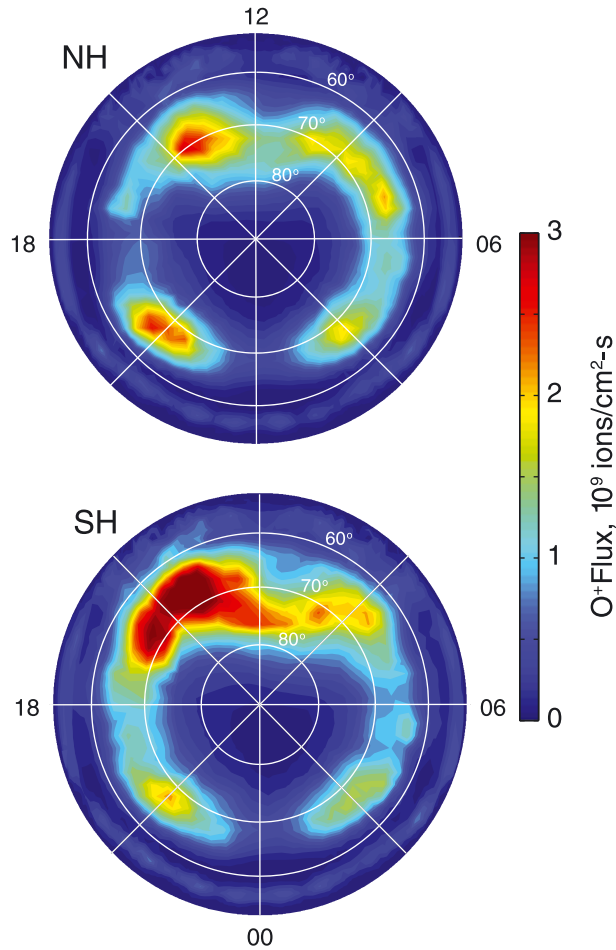


**Figure 10.** Daily average of the outflow flux mapped to a reference altitude of 100 km in (top) northern hemisphere and (bottom) southern hemisphere during 24 October 2002 sawtooth event.

The hemispheric outflow rate from the southern, summer hemisphere is generally larger than the northern, winter hemisphere, which is consistent with the results from the simulated 18 April 2002 storm.

[34] The morphology of the average daily outflow flux for the simulation is shown in Figure 10. Hourly averages show a similar pattern to the daily average since the IMF varies in a consistent manner throughout the day. However, the magnitude of the outflow flux varies with the magnitude of the oscillating IMF. The outflow is located throughout the auroral oval with nightside peaks in both the pre-midnight and postmidnight sectors at approximately  $67^\circ$  MLAT. A greater outflow flux is generated on the dayside for the SIR event than in the simulated ICME event, a consequence of the more variable solar wind conditions during the SIR event. The resulting variability along the dayside magnetopause boundary stimulates Alfvén waves propagating to low altitude on the dayside. This Alfvénic power drives a dayside outflow flux in the simulation that is larger than the nightside outflow flux, with similar morphology in both the northern and southern hemisphere. The increase in hemispheric outflow rate in the southern hemisphere is due to a larger magnitude of outflow flux in the southern hemisphere, rather than an increased area of flux. The peak outflow flux in the northern hemisphere is  $2.3 \times 10^9 \text{ O}^+ / \text{cm}^2/\text{s}$  compared to  $3.5 \times 10^9 \text{ O}^+ / \text{cm}^2/\text{s}$  in the southern hemisphere.

#### 4.2. Results

[35] The 24 October 2002 storm produced eight particle injections at LANL geostationary satellites that *Huang et al.* [2004] associated with substorms. Four of these substorms satisfy the *Cai and Clauer* [2009] conditions for a sawtooth substorm. Table 2 lists the 8(4) onset timings. In contrast to the 18 April 2002 event, this event has not been studied in great detail. During this event Geotail was located in the solar wind and therefore cannot be used to calculate the magnetotail open flux as for the 18 April 2002 event. The timings of the simulated substorms, estimated using the open flux in the polar cap and magnetic fields in the tail will be compared to timings of the observed substorms from the LANL data. In addition, the magnetic fields in the simulation will be compared to the magnetic fields observed from GOES 8 and 10.

[36] Figure 11 shows the polar cap magnetic flux from the baseline and outflow simulations, calculated using the same method as for the simulated 18 April 2002 storm. The open

**Table 2.** Onset Times for the 24 October 2002 Sawtooth Event From Observations Reported by *Cai and Clauer* [2009] and *Huang et al.* [2004], Baseline Simulation and Outflow Simulation<sup>a</sup>

Sawtooth Number	Observed Onset (UT) [ <i>Cai and Clauer</i> , 2009]	Observed Onset (UT) [ <i>Huang et al.</i> , 2004]	Baseline Onset (UT)	Outflow Onset (UT)
1			0158 (0210)	0156 (0210)
2		0359	0355 (0405)	0352
3	0542	0545	0530 (0600)	0538 (0600)
4			0702	0702
5		0859	0849 (0920)	(0912)
6	1052	1054	1042 (1100)	1042 (1100)
7			1205 (1205)	1207 (1200)
8	1403	1400	1355 (1340)	1401 (1340)
9			1500	1508
10	1638	1648	1650 (1645)	1708 (1642)
11		1900	1848	1854 (1835)
12			2005 (1940)	2005 (1954)
13		2127	2127	2121 (2110)

<sup>a</sup>Onset times for baseline and outflow simulations are calculated using the open magnetic flux in the polar cap. Onset times using magnetic fields at  $9 R_E$  in the nightside magnetosphere are enclosed in parentheses.

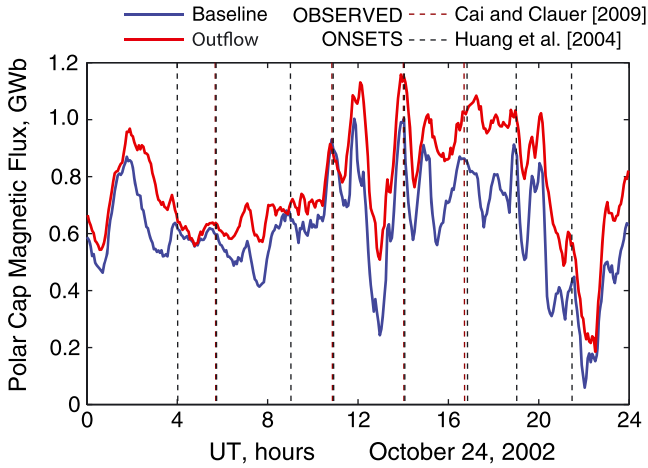


**Figure 11.** Open magnetic flux in the polar cap derived from the baseline simulation (blue) and outflow simulation (red) during the 24 October 2002 sawtooth event. Red vertical dashed lines show substorm onsets reported by *Cai and Clauer* [2009] and black vertical dashed lines show observed substorm onsets reported by *Huang et al.* [2004].

magnetic flux derived from observations is not available for this event. The onsets of the observed substorms identified by *Huang et al.* [2004] are marked on the plot by vertical black dashed lines. The subset of four onsets designated by *Cai and Clauer* [2009] as sawtooth substorms are indicated by vertical red dashed lines. The simulated open flux in the polar cap when outflow is included has a similar profile to the baseline simulation. Both the baseline and outflow simulations capture a sequence of 12–13 increases and decreases of open magnetic flux which may be related to substorm activity (see Table 2). It is difficult to discern whether the decreases in open magnetic flux relate to substorm activity or smaller nightside activations. A number of simulated nightside activities occur at times that are consistent with the timings of the observed substorm onsets (Table 2). In contrast with the simulated 18 April 2002 event, the inclusion of outflow does not significantly affect the generation and timings of the substorms. Periods of loading and unloading of open magnetic flux, consistent with substorms, occur regardless of whether or not outflow is included. Since simulated baseline and outflow substorms and observed substorms occur at similar times, it is likely that the generation of the substorms during this event is controlled by the solar wind. One notable difference in the time history of the open flux in the baseline and outflow simulations is that the open magnetic flux is approximately 0.1 Gwb larger when outflow is included.

[37] Figure 12 shows the magnetic inclination angle at three locations (2100 MLT, 0000 MLT, and 0300 MLT) at a radius of  $9 R_E$  in the SM equatorial plane for the baseline and outflow simulations. The vertical black dashed lines show the timings of the observed substorms reported by [*Cai and Clauer*, 2009] and the vertical red dashed lines denote the timings reported by [*Huang et al.*, 2004]. Both baseline and outflow simulations show dipolarizations in the inner magnetosphere that are consistent with the timings of the observed sawteeth onsets (Table 2).

Although some variation is evident between the profiles, the timings of the dipolarizations between the baseline and outflow simulations are relatively consistent with each other. However, at substorm onset, the simulation with outflow shows a greater degree of magnetic field stretching than in the baseline simulation. For example, the magnetic inclination angle for the substorm occurring at 1400 UT is lower at all of the examined locations when outflow is included. These substorms are especially more intense after 1200 UT when the hemispheric outflow rate is larger. While outflow has not affected the timings of the substorms, the intensity of the substorms has increased when outflow is included, exhibiting the characteristic signatures of sawteeth.

[38] Figure 13 shows a comparison of the magnetic fields observed by GOES 8 and 10 and the simulated magnetic fields at the location of GOES 8 and 10. In general, the simulation captures the overall profiles of both  $B_x$  and  $B_y$  reasonably well but does worse with  $B_z$ . The poor agreement between the simulated and observed values of  $B_z$  is probably due to the weaker simulated ring current [*Brambles et al.*, 2010]. The sharp decreases in the simulated magnetic field when the satellites are on the dayside are probably due to the close proximity of the magnetopause during these times. The simulated location of the magnetopause in the LFM simulation is generally earthwards of the observed position [*Garcia and Hughes*, 2007].

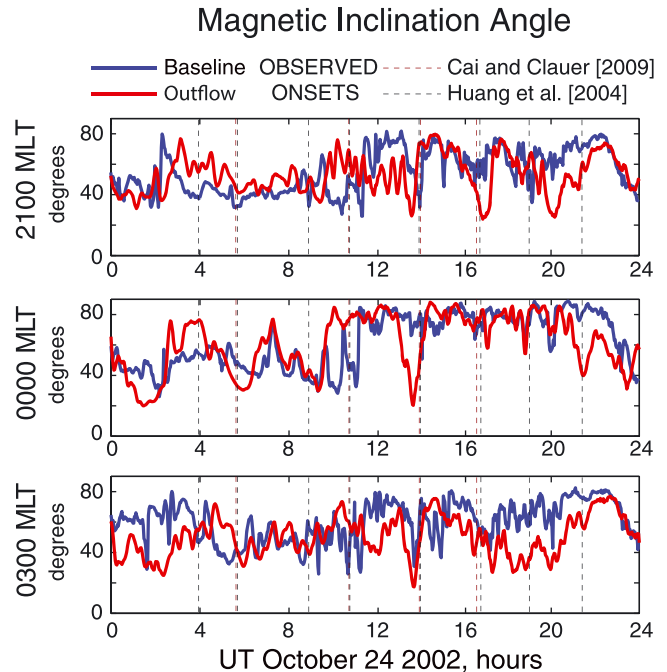


**Figure 12.** Magnetic inclination angle calculated at  $9 R_E$  in the SM equatorial plane at (top) 2100 UT, (middle) 0000 UT, and (bottom) 0300 MLT for the baseline simulation (blue) and outflow simulation (red) during the 24 October 2002 sawtooth event. Red vertical dashed lines show substorm onsets reported by *Cai and Clauer* [2009]. Black vertical dashed lines show observed substorm onsets reported by *Huang et al.* [2004].

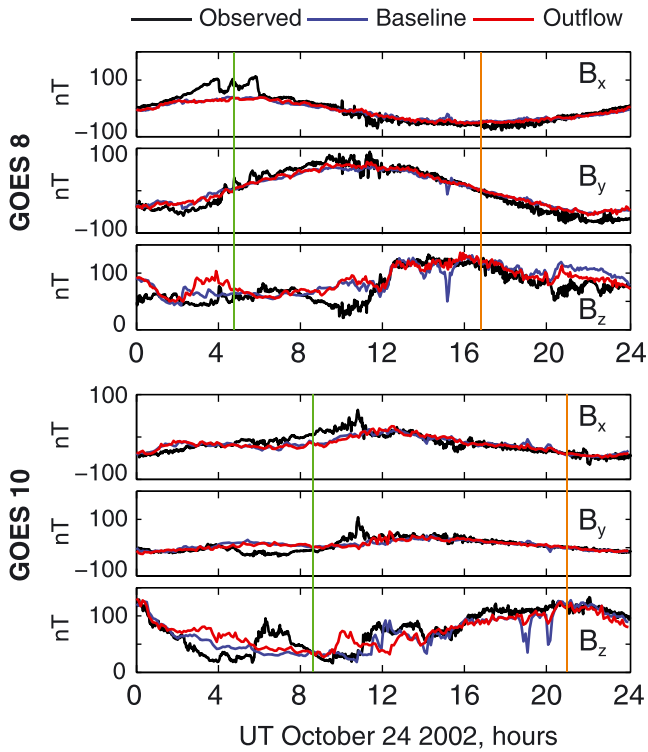


**Figure 13.** Comparison of magnetic field taken at GOES 8 and 10 (black) with simulated magnetic fields at GOES 8 and 10 for baseline (blue) and outflow (red) simulations during the 24 October 2022 sawtooth event. Vertical green and orange denote the times when the satellite passed through GSM midnight and noon, respectively.

## 5. Discussion

[39] Outflow was required to produce simulated quasi-periodic substorms for the ICME-driven event on 18 April 2002 but not for the SIR-driven 24 October 2002 event. In the baseline simulation of the 18 April 2002 ICME-driven event, the MI system settles into a quasi-steady mode of convection after an initiating substorm. When ionospheric outflow is included in the simulation, the convection becomes quasi-periodic and recurring substorms are observed. In contrast, during the simulated SIR event, ionospheric outflow does not significantly affect the dynamics of magnetospheric convection. Quasi-periodic substorms are observed regardless of whether outflow is included or not in the simulation. Therefore, the mechanisms that generate the substorms during the SIR-driven event must be different than in the ICME-driven event.

[40] The periodic substorms during both the SIR-driven and ICME-driven events are characterized by the loading and unloading of open magnetic flux. The results from Huang *et al.* [2009] suggest that sawtooth onset can only occur when the open magnetic flux in the magnetosphere has reached a critical level. Near the critical level, instabilities may be triggered internally or externally by changes in the solar wind which result in substorm onset [Huang, 2011]. In order for the open magnetic flux to increase to this critical level, the dayside reconnection potential must be larger than the nightside reconnection potential. In the

baseline simulation for the 18 April 2002 event, the growth in open magnetic flux in the first substorm in the simulation is caused by the change in IMF  $B_z$  from positive to negative at 0030 UT. Flux is opened by dayside merging and transported to the tail where it is not immediately reconnected. As the open flux nears the critical level, the magnetosphere becomes susceptible to internal instabilities. The increase in solar wind dynamic pressure at 0200 UT likely triggers an internal instability which results in substorm onset. In the outflow simulation, the open flux grows at a faster rate than in the baseline simulation suggesting that the growth is from a combination of the increase in dayside merging and a decrease in nightside reconnection due to the  $O^+$  outflow [Ouellette *et al.*, 2013]. The exact trigger of this substorm in the outflow simulation is difficult to determine. To what extent the substorm is triggered by the increase in dynamic pressure or solely via the internal processes induced by the  $O^+$  ions requires further study using finer grid and time resolution. Since the observed initial substorm and the initial substorm in the baseline and outflow simulation all occur at similar times, it can be assumed that the dynamics of the first substorm in the sawtooth sequence is largely controlled by the solar wind.

[41] After the IMF turns southward at 0030 on 18 April 2002, there are no further changes in the direction of IMF  $B_z$ . After the first substorm in the baseline simulation, the magnetosphere reconfigures such that the nightside is able to reconnect flux on average at the same rate at which it is opened on the dayside. However, the reconnection on the nightside is time variable resulting in an active SMC mode. In the outflow simulation, as the  $O^+$  accumulates in the plasma sheet, nightside reconnection is reduced [Ouellette *et al.*, 2013], which results in a growth of open magnetic flux. When the open flux reaches a critical level, an internal instability evidently triggers sawtooth onset. An  $O^+$ -rich plasmoid is ejected from the tail and the magnetic field dipolarizes. This process repeats throughout the day with an average period of approximately 2.75 h manifested in the sawtooth oscillation mode. The sequence of onsets of sawtooth substorms in the outflow simulation is delayed by approximately 1.3 h relative to the observed onsets. This result suggests that the substorm growth and triggering are largely caused by internal dynamics rather than changes in the solar wind. Had the substorm been triggered by the solar wind, the difference in timings between observed and simulated substorms would be reduced. In order to improve the accuracy of the timings of the sawtooth onsets, it will be necessary to improve both the outflow model and the physics of reconnection and convection in the magnetosphere.

[42] In the SIR-driven event, the changes in open magnetic flux are driven largely by the variability in the solar wind. This fact is evidenced by the similarities between the baseline and outflow simulations. When IMF  $B_z$  continually fluctuates between positive and negative, the dayside and nightside reconnection potentials cannot be balanced leading to the asymmetric transfer of magnetic flux in the magnetosphere. This imbalance can cause open magnetic flux to accumulate in the tail and grow to a critical level at which point an instability triggers substorm onset. This variability in the solar wind has a larger impact on the dynamics of magnetospheric convection than the ionospheric outflow. When the magnetosphere is driven by a sufficiently

large (and steady) southward IMF, the magnetosphere settles into an intrinsic period of 2–4 h which is governed by the ionospheric outflow. In the SIR-driven event, the external modulation of the solar wind overrides this effect, and the periodic dynamics of magnetospheric convection are controlled by the solar wind.

[43] Sawtooth oscillations are characterized by quasi-global signatures. In these simulations, the ionospheric outflow significantly affects the signatures of the substorms. In the simulated 18 April 2002, the accumulation of  $O^+$  ions in the plasma sheet and inner magnetosphere stretch the nightside field lines in the outflow simulation to a greater extent. While the first substorm is generated through the modulation in the IMF, in the outflow simulation, the signatures are more intense: the minimum tilt angle is lower, the MLT range over which the substorm is observed is larger, and the magnetic flux at onset is larger. In the baseline simulation, the signatures are consistent with an isolated substorm and in the outflow simulation, they are similar to a sawtooth substorm. In the outflow simulation for the 18 April 2002 event, the dynamics of the first substorm are generally controlled through the changes in the solar wind while the subsequent substorms are controlled solely through the interaction of the outflow with the nightside magnetosphere. However, the signatures of substorms 2–7 share the same general characteristics and signatures of the first substorm in the outflow simulation at 0218 UT.

[44] In the outflow simulations, the  $O^+/H^+$  pressure ratio in the plasma sheet ranges from approximately 0.1 to 30 depending upon the location and simulation time. For example, at 0200 UT on 18 April 2002, the  $O^+/H^+$  pressure ratio is 1–2 at  $x_{SM} = -20 R_E$ . After 0400UT, when the solar wind number density decreases to 1–2  $/cm^3$ , the pressure ratio increases to over 10. These values are greater than the pressure ratio of 0.6 found for a superposed epoch analysis of storm time substorms using CLUSTER data [Kistler *et al.*, 2006]. However, for substorms that occurred during the 1 October 2001 and 17 August 2001 storms, Kistler *et al.* [2005] found times when  $O^+$  dominated both the ion pressure and number density in the plasma sheet resulting in  $O^+/H^+$  pressure ratios of over 10, consistent with the simulation results. These substorms were later identified as sawtooth substorms by Cai and Clauer [2009]. In addition, the  $O^+$  pressure in the simulated 18 April 2002 event (0.05–0.3 nPa at  $x_{SM} = -19 R_E$ ) is consistent with the  $O^+$  pressure observed by Kistler *et al.* [2005] (0.2–0.4 nPa at  $19 R_E$  in the tail) for the 1 October 2001 event. Both of these sawtooth events were classed as moderate storms and had a similar minimum Dst (–130 nT on 18 April 2002 and –150 nT on 1 October 2001).

[45] It is not unreasonable to expect large  $O^+/H^+$  number density and pressure ratios during sawtooth events when typically the solar wind number density is low and the geomagnetic activity is high [DeJong *et al.*, 2009; Cai and Clauer, 2009]. The low solar wind number density will produce a low  $H^+$  density in the plasma sheet [Borovsky *et al.*, 1998] and the high geomagnetic activity will generate a large flux of  $O^+$  [Lennartsson *et al.*, 2004]. However, it is probable that the simulated  $O^+/H^+$  pressure ratio is too large. In the simulation, the inclusion of  $O^+$  outflow acts to exclude  $H^+$  from the plasma sheet and inner magnetosphere [Brambles *et al.*, 2010; Winglee *et al.*, 2005], inflating the

$O^+/H^+$  pressure ratio. The simulated  $H^+$  pressure in the plasma sheet drops by a factor of 3–10 when outflow is included. Second, it is anticipated that the inclusion of an  $H^+$  outflow to the global simulation would increase the  $H^+$  pressure in the plasma sheet and reduce the  $O^+/H^+$  pressure ratio.

[46] In the SIR-driven event, the ionospheric outflow also affects the signatures of the substorms. When outflow is included, the open magnetic flux increases and the inclination angle at substorm onset is decreased across a range of magnetic local times. The signatures of the substorms with outflow appear closer to observed sawteeth while the signatures of substorms when outflow is not included are more comparable to observed isolated substorms. This scenario is similar to the first substorm during the 18 April 2002 event where the substorm is generated by the solar wind, but the addition of ionospheric outflow changes the signatures of the substorms.

[47] This result suggests that the intensity of the substorm at geostationary orbits depends upon the accumulation of  $O^+$  in the inner magnetosphere and plasma sheet. It is therefore not surprising that signatures of sawtooth substorms show similarities to a subset of storm time substorm activations [Pulkkinen *et al.*, 2007]. Storms which are driven by high solar wind driving are likely to produce a large hemispheric outflow rate of  $O^+$  ions which accumulates in the plasma sheet. Therefore, storm time activations will also exhibit the intense, widespread features associated with sawtooth oscillations. In a similar manner, the periodic substorms that occur during High Speed Streams (HSS) have signatures consistent with classic, isolated substorms. During HSS the fluctuating IMF and hemispheric outflow rate is typically weaker than during both the 24 October 2002 and 18 April 2002 events. The weaker ionospheric outflow will not produce the level of field line stretching in the nightside, and therefore, the signatures of these periodic substorms will be like classic, isolated substorms rather than sawtooth substorms.

## 6. Conclusion

[48] The results of this paper suggest that the mechanism that generated the sawtooth substorms cannot be determined based solely on quasi-global signatures of substorms at geostationary satellites. In fact, not all sawtooth substorms represent the same physical processes. The event simulations presented here show that substorm signatures in the geostationary region are a feature of the large accumulation of ionospheric outflow in the inner magnetosphere and plasma sheet. It is impossible to determine how the substorms are generated and triggered through the sole examination of these signatures. While the signatures of sawtooth events driven by ICMEs and SIR are similar, the mechanisms that generate them are different. The sawteeth generated by ICME-driven steady solar wind conditions are a response of the MI system to an intrinsic internal cycle controlled by the latency in the transit of ionospheric outflows between the ionosphere and plasma sheet and the resulting inflation rate of the plasma sheet [Ouellette *et al.*, 2013], while the periodicity of substorms generated by SIR-driven fluctuations are controlled primarily by the external modulation of the IMF.

[49] **Acknowledgments.** The research was supported by NASA under Heliophysics Theory Program Grant NNX11AO59G and Geospace Supporting Research and Technology grant NNX11AJ10G, by the NSF National Space Weather Program grant AGS-1023346, and by the Center for Integrated Space Weather Modeling funded by the NSF Science and Technology Centers program under cooperative agreement ATM-0120950. The National Center for Atmospheric Research is sponsored by the National Science Foundation. Computing resources for the research were provided by the National Center for Atmospheric Research under CISL projects 36761008 and 3761009.

[50] Robert Lysak thanks Xia Cai and another reviewer for their assistance in evaluating this paper.

## References

- Baumjohann, W., G. Paschmann, and H. Luhr (1990), Pressure balance between lobe and plasma sheet, *Geophys. Res. Lett.*, *17*(1), 45–48, doi:10.1029/GL017i001p00045.
- Belian, R. D., T. E. Cayton, and G. D. Reeves (1995), *Quasi-Periodic Global Substorms Generated Flux Variations Observed at Geosynchronous Orbit*, vol. 86, AGU, Washington D.C.
- Bouhram, M., B. Klecker, W. Miyake, H. Rème, J.-A. Sauvaud, M. Malingre, L. Kistler, and A. Blågäu (2004), On the altitude dependence of transversely heated O<sup>+</sup> distributions in the cusp/cleft, *Ann. Geophys.*, *22*, 1787–1798.
- Borovsky, J. E., R. J. Nemzek, and R. D. Belian (1993), The occurrence rate of magnetospheric substorm onsets: Random and periodic substorms, *J. Geophys. Res.*, *98*(A3), 3807–3813, doi:10.1029/92ja02556.
- Borovsky, J. E., M. F. Thomsen, and R. C. Elphic (1998), The driving of the plasma sheet by the solar wind, *J. Geophys. Res.*, *103*(A8), 17,617–17,639, doi:10.1029/97JA02986.
- Brambles, O. J., W. Lotko, P. A. Damiano, B. Zhang, M. Wiltberger, and J. Lyon (2010), Effects of causally driven cusp O<sup>+</sup> outflow on the storm time magnetosphere-ionosphere system using a multifluid global simulation, *J. Geophys. Res.*, *115*, A00J04, doi:10.1029/2010JA015469.
- Brambles, O. J., W. Lotko, B. Zhang, J. Lyon, M. Wiltberger, and R. J. Strangeway (2011), Magnetosphere sawtooth oscillations induced by ionospheric outflow, *Science*, *332*, 1183–1186, doi:10.1126/science.1202869.
- Brambles, O. J. (2012), The effects of ionospheric outflow on the dynamics of magnetospheric convection, PhD thesis, Thayer Sch. of Eng., Dartmouth Coll., Hanover, N.H. [Available at <http://libarchive.dartmouth.edu/cdm/compoundobject/collection/dcdis/id/88624>].
- Cai, X., M. G. Henderson, and C. R. Clauer (2006), A statistical study of magnetic dipolarization for sawtooth events and isolated substorms at geosynchronous orbit with GOES data, *Ann. Geophys.*, *24*, 3481–3490.
- Cai, X., and C. R. Clauer (2009), Investigation of the period of sawtooth events, *J. Geophys. Res.*, *114*, A06201, doi:10.1029/2008ja013764.
- Chaston, C. C., J. W. Bonnell, C. W. Carlson, J. P. McFadden, R. E. Ergun, R. J. Strangeway, and E. J. Lund (2004), Auroral ion acceleration in dispersive Alfvén waves, *J. Geophys. Res.*, *109*, A04205, doi:10.1029/2003ja010053.
- Chaston, C. C., C. W. Carlson, J. P. McFadden, R. E. Ergun, and R. J. Strangeway (2007), How important are dispersive Alfvén waves for auroral particle acceleration? *Geophys. Res. Lett.*, *34*, L07101, doi:10.1029/2006gl029144.
- Dang, G., S. Y. Ma, and Y. L. Zhou (2007), Morphology of polar ionospheric O<sup>+</sup> ion upflow: FAST observations during quiet time, *Chinese Sci. Bull.*, *52*, 3403–3415, doi:10.1007/s11434-007-0444-1.
- DeJong, A. D., A. J. Ridley, and C. R. Clauer (2008), Balanced reconnection intervals: Four case studies, *Ann. Geophys.*, *26*, 3897–3912.
- DeJong, A. D., A. J. Ridley, X. Cai, and C. R. Clauer (2009), A statistical study of BRIs (SMCs), isolated substorms, and individual sawtooth injections, *J. Geophys. Res.*, *114*, A08215, doi:10.1029/2008ja013870.
- Fedder, J. A., S. P. Slinker, J. G. Lyon, and R. D. Elphinstone (1995), Global numerical simulation of the growth phase and the expansion onset for a substorm observed by Viking, *J. Geophys. Res.*, *100*(A10), 19,083–19,093, doi:10.1029/95ja01524.
- Garcia, K. S., and W. J. Hughes (2007), Finding the Lyon-Fedder-Mobarry magnetopause: A statistical perspective, *J. Geophys. Res.*, *112*, A06229, doi:10.1029/2006JA012039.
- Garcia, K. S., V. G. Merkin, and W. J. Hughes (2010), Effects of nightside O<sup>+</sup> outflow on magnetospheric dynamics: Results of multifluid MHD modeling, *J. Geophys. Res.*, *115*, A00J09, doi:10.1029/2010ja015730.
- Glocer, A., G. Toth, T. Gombosi, and D. Welling (2009a), Modeling ionospheric outflows and their impact on the magnetosphere, initial results, *J. Geophys. Res.*, *114*, A05216, doi:10.1029/2009ja014053.
- Glocer, A., G. Toth, Y. Ma, T. Gombosi, J. C. Zhang, and L. M. Kistler (2009b), Multifluid block-adaptive-tree solar wind roe-type upwind scheme: Magnetospheric composition and dynamics during geomagnetic storms—initial results, *J. Geophys. Res.*, *114*, A12203, doi:10.1029/2009ja014418.
- Goodrich, C. C., T. I. Pulkkinen, J. G. Lyon, and V. G. Merkin (2007), Magnetospheric convection during intermediate driving: Sawtooth events and steady convection intervals as seen in Lyon-Fedder-Mobarry global MHD simulations, *J. Geophys. Res.*, *112*, A08201, doi:10.1029/2006ja012155.
- Henderson, M. G., G. D. Reeves, R. Skoug, M. F. Thomsen, M. H. Denton, S. B. Mende, and H. J. Singer (2006), Magnetospheric and auroral activity during the 18 April 2002 sawtooth event, *J. Geophys. Res.*, *111*, A01S90, doi:10.1029/2005ja011111.
- Huang, C.-S., G. D. Reeves, J. E. Borovsky, R. M. Skoug, Z. Y. Pu, and G. Le (2003), Periodic magnetospheric substorms and their relationship with solar wind variations, *J. Geophys. Res.*, *108*(A6), 1255, doi:10.1029/2002ja009704.
- Huang, C.-S., G. D. Reeves (2004), Periodic magnetospheric substorms during fluctuating interplanetary magnetic field Bz, *Geophys. Res. Lett.*, *31*, L14801, doi:10.1029/2004GL020180.
- Huang, C.-S., A. D. DeJong, and X. Cai (2009), Magnetic flux in the magnetotail and polar cap during sawteeth, isolated substorms, and steady magnetospheric convection events, *J. Geophys. Res.*, *114*, A07202, doi:10.1029/2009ja014232.
- Huang, C., and X. Cai (2009), Magnetotail total pressure and lobe magnetic field at onsets of sawtooth events and their relation to the solar wind, *J. Geophys. Res.*, *114*, A04204, doi:10.1029/2008JA013807.
- Huang, C.-S. (2011), Relation between magnetotail magnetic flux and changes in the solar wind during sawtooth events: Toward resolving the controversy of whether all substorm onsets are externally triggered, *J. Geophys. Res.*, *116*, A04202, doi:10.1029/2010JA016371.
- Hultqvist, B., H. Vo, R. Lundin, B. Aparicio, P.-A. Lindqvist, G. Gustafsson, and B. Holback (1991), On the upward acceleration of electrons and ions by low-frequency electric-field fluctuations observed by VIKING, *J. Geophys. Res.*, *96*(A7), 11,609–11,615, doi:10.1029/91ja01057.
- Hultqvist, B., M. Oieroset, G. Paschmann, and R. Treumann (eds.) (1999), *Magnetospheric Plasma Sources and Losses*, Springer, New York.
- Kamide, Y., and E. W. Kroehl (1993), Auroral electrojet activity during isolated substorms at different local times: A statistical study, *Geophys. Res. Lett.*, *21*(5), 389–392, doi:10.1029/GL021i005p00389.
- Keiling, A., J. R. Wygant, C. A. Cattell, F. S. Mozer, and C. T. Russell (2003), The global morphology of wave Poynting flux: Powering the aurora, *Science*, *299*(5605), 383–386, doi:10.1126/science.1080073.
- Kitamura, K., H. Kawano, S. Ohtani, A. Yoshikawa, and K. Yumoto (2005), Local time distribution of low and middle latitude ground magnetic disturbances at sawtooth injections of 18–19 April 2002, *J. Geophys. Res.*, *110*(A7), A07208, doi:10.1029/2004ja010734.
- Kistler, L. M., et al. (2005), Contribution of nonadiabatic ions to the cross-tail current in an O<sup>+</sup> dominated thin current sheet, *J. Geophys. Res.*, *110*, A06213, doi:10.1029/2004JA010653.
- Kistler, L. M., et al. (2006), Ion composition and pressure changes in storm time and nonstorm substorms in the vicinity of the near-Earth neutral line, *J. Geophys. Res.*, *111*, A11222, doi:10.1029/2006JA011939.
- Klumpar, D. M. (1979), Transversely accelerated ions: An ionospheric source of hot magnetospheric ions, *J. Geophys. Res.*, *84*, 4229–4237, doi:10.1029/JA084iA08p04229.
- Lee, D.-Y., et al. (2006), Repetitive substorms caused by Alfvén waves of the interplanetary magnetic field during high-speed solar wind streams, *J. Geophys. Res.*, *111*, A12214, doi:10.1029/2006JA011685.
- Lennartsson, O. W., H. L. Collin, and W. K. Peterson (2004), Solar wind control of Earth's H<sup>+</sup> and O<sup>+</sup> outflow rates in the 15-eV to 33-keV energy range, *J. Geophys. Res.*, *109*, A12212, doi:10.1029/2004ja010690.
- Lyon, J. G., J. A. Fedder, and C. M. Mobarry (2004), The Lyon-Fedder-Mobarry (LFM) global MHD magnetospheric simulation code, *J. Atmos. Sol. Terr. Phys.*, *66*, 1333–1350, doi:10.1016/j.jastp.2004.03.020.
- McPherron, R., T. P. O'Brien, and S. M. Thompson (2008), *Multiscale Coupling of Sun-Earth Processes*, Elsevier, Amsterdam.
- Norqvist, P., M. Andre, and M. Tyrland (1998), A statistical study of ion energization mechanisms in the auroral region, *J. Geophys. Res.*, *103*(A10), 23,459–23,473, doi:10.1029/98ja02076.
- Nosé, M., S. Taguchi, S. P. Christon, M. R. Collier, T. E. Moore, C. W. Carlson, and J. P. McFadden (2009), Response of ions of ionospheric origin to storm time substorms: Coordinated observations over the ionosphere and in the plasma sheet, *J. Geophys. Res.*, *114*, A05207, doi:10.1029/2009JA014048.
- O'Brien, T. P., S. M. Thompson, and R. L. McPherron (2002), Steady magnetospheric convection: Statistical signatures in the solar wind and AE, *Geophys. Res. Lett.*, *29*(7), 1130, doi:10.1029/2001gl014641.

- Ouellette, J., O. J. Brambles, W. Lotko, B. Rogers, B. Zhang, M. Wiltberger, and J. Lyon (2013), Properties of outflow-driven sawtooth substorms, *J. Geophys. Res. Space Phys.*, *118*, 3223–3232, doi:10.1002/jgra.50309.
- Peterson, W. K., L. Andersson, B. C. Callahan, H. L. Collin, J. D. Scudder, and A. W. Yau (2008), Solar-minimum quiet time ion energization and outflow in dynamic boundary related coordinates, *J. Geophys. Res.*, *113*, A07222, doi:10.1029/2008ja013059.
- Pulkkinen, T. I., N. Partamies, K. E. J. Huttunen, G. D. Reeves, and H. E. J. Koskinen (2007), Differences in geomagnetic storms driven by magnetic clouds and ICME sheath regions, *Geophys. Res. Lett.*, *34*, L02105, doi:10.1029/2006gl027775.
- Robinson, R. M., R. R. Vondrak, K. Miller, T. Dabbs, and D. Hardy (1987), On calculating ionospheric conductances from the flux and energy of precipitating electrons, *J. Geophys. Res.*, *92*(A3), 2565–2569, doi:10.1029/JA092iA03p02565.
- Sergeev, V. A., and W. Lennartsson (1988), Plasma sheet at  $x \sim -20 R_E$  during steady magnetospheric convection, *Planet. Space Sci.*, *36*(4), 353–370, doi:10.1016/0032-0633(88)90124-9.
- Seyler, C. E., and K. Liu (2007), Particle energization by oblique inertial Alfvén waves in the auroral region, *J. Geophys. Res.*, *112*, A09302, doi:10.1029/2007ja012412.
- Shelley, E. G., R. D. Sharp, and R. G. Johnson (1976), Satellite observations of an ionospheric acceleration mechanism, *Geophys. Res. Lett.*, *3*(11), 654–656, doi:10.1029/GL003i011p00654.
- Shue, J.-H., J. K. Chao, H. C. Fu, C. T. Russell, P. Song, K. K. Khurana, and H. J. Singer (1997), A new functional form to study the solar wind control of the magnetopause size and shape, *J. Geophys. Res.*, *102*(A5), 9497–9511, doi:10.1029/97JA00196.
- Spence, H. E., M. G. Kivelson, R. J. Walker, and D. J. McComas (1989), Magnetospheric plasma pressure in the midnight meridian: Observations from 2.5 to 35  $R_E$ , *J. Geophys. Res.*, *94*(A5), 5264–5272, doi:10.1029/JA094iA05p05264.
- Thelin, B., B. Aparicio, and R. Lundin (1990), Observations of upflowing ionospheric ions in the mid-altitude cusp/cleft region with the VIKING satellite, *J. Geophys. Res.*, *95*(A5), 5931–5939, doi:10.1029/JA095iA05p05931.
- Troshichev, O., and A. Janzhura (2009), Relationship between the PC and AL indices during repetitive bay-like magnetic disturbances in the auroral zone, *J. Atmos. Sol. Terr. Phys.*, *71*, 1340–1352, doi:10.1016/j.jastp.2009.05.017.
- Tung, Y. K., C. W. Carlson, J. P. McFadden, D. M. Klumpar, G. Parks, W. J. Peria, and K. Liou (2001), Auroral polar cap boundary ion conic outflow observed on FAST, *J. Geophys. Res.*, *106*(A3), 3603–3614, doi:10.1029/2000ja900115.
- Whalen, B. A., W. Bernstein, and P. W. Daly (1978), Low-altitude acceleration of ionospheric ions, *Geophys. Res. Lett.*, *5*(1), 55–58, doi:10.1029/GL005i001p00055.
- Wiltberger, M., R. S. Weigel, W. Lotko, and J. A. Fedder (2009), Modeling seasonal variations of auroral particle precipitation in a global-scale magnetosphere-ionosphere simulation, *J. Geophys. Res.*, *114*, A01204, doi:10.1029/2008ja013108.
- Wiltberger, M., W. Lotko, J. G. Lyon, P. Damiano, and V. Merkin (2010), Influence of cusp  $O^+$  outflow on magnetotail dynamics in a multifluid MHD model of the magnetosphere, *J. Geophys. Res.*, *115*, A00J05, doi:10.1029/2010ja015579.
- Winglee, R. M., W. Lewis, and G. Lu (2005), Mapping of the heavy ion outflows as seen by IMAGE and multifluid global modeling for the 17 April 2002 storm, *J. Geophys. Res.*, *110*, A12S24, doi:10.1029/2004JA010909.
- Yau, A. W., and M. André (1997), Sources of ion outflow in the high latitude ionosphere, *Space Sci. Rev.*, *80*(1-2), 1–25, doi:10.1023/a:1004947203046.
- Zhang, B., W. Lotko, O. Brambles, P. Damiano, M. Wiltberger, and J. Lyon (2012), Magnetotail origins of auroral Alfvénic power, *J. Geophys. Res.*, *117*, A09205, doi:10.1029/2012JA017680.